



Enhancing photocatalytic H₂O₂ production through the improvement of water oxidation via a novel lattice-oxygen-involved pathway

Chaofeng Chen^{a,b}, Chen Wang^c, Yaning Zhang^{a,b}, Hao Sun^{a,b}, Jing Xu^d, Ying Zhang^{a,b}, Yang Lou^{a,b}, Yongfa Zhu^e, Chengsi Pan^{a,b,*}

^a Key Laboratory of Synthetic and Biological Colloids, Ministry of Education, School of Chemical and Material Engineering, Jiangnan University, Wuxi, Jiangsu 214122, China

^b International Joint Research Center for Photoresponsive Molecules and Materials, Jiangnan University, Wuxi, Jiangsu 214122, China

^c Harbin Zhongke Materials Engineering Co., Ltd, Harbin 150040, China

^d School of Food Science and Technology, Jiangnan University, Wuxi, Jiangsu 214122, China

^e Department of Chemistry, Tsinghua University, Beijing 100084, China

ARTICLE INFO

Keywords:

Photocatalysis • Bi vacancies • Nanocrystal • Peroxides • Antibiotics

ABSTRACT

Bi-vacancy-rich BiPO₄ nanocrystals (V_{Bi}-BIP) have achieved high H₂O₂ production, providing an in-situ source for UV/H₂O₂ degradation. These nanocrystals produce H₂O₂ at 26.7 mM·g⁻¹·h⁻¹, surpassing most inorganic and organic photocatalysts, and have an AQY of 43.4% and ECE of 10.7% at 254 ± 10 nm. The Bi vacancies enhance activity by enabling a new lattice-oxygen-involved pathway for H₂O₂ formation, with a potential 0.34 V lower than conventional water oxidation reactions. Using in-situ generated H₂O₂ on V_{Bi}-BIP, organic pollutants can be efficiently degraded, achieving a 92% removal rate for ciprofloxacin in a flow reactor operated at 2.4 L/h for 400 hours. The energy cost per unit of treated water (EE/O) in this in-situ degradation device is 0.58 kWh/m³, half of that in traditional UV/H₂O₂ treatment. The creation of cation vacancies and their function elucidation for H₂O₂ generation paves the way for designing more efficient photocatalysts for in-situ H₂O₂ use in the future.

1. Introduction

As one of the most extensively studied advanced oxidation processes (AOPs), UV/H₂O₂ degradation technology has been established since 1955 [1–3]. In recent years, this technology has been practically applied in the field of drinking water treatment [4,5] and exhibits potential applications in the treatment of industrial effluent and feedwater because of its eco-economic feasibility and simplicity in the treatment process [6,7]. This technology completely removes pollutants in water by producing strong oxidizing hydroxyl radicals (HO•, E=2.80 V) from the cleavage of O–O bonds in H₂O₂ [6,8]. The reaction has a theoretical 100% quantum yield of HO• generation [9]. However, the low UV absorption of H₂O₂ (ε_{254 nm}=18.6 M⁻¹ cm⁻¹) results in inefficient production of HO• and high energy consumption [10]. The addition of exogenous H₂O₂ further limits its application due to the potential hazards associated with the transport, storage, and handling of bulk H₂O₂, as well as the additional costs involved [11].

In the UV/H₂O₂ method, complete removal of organic pollutants can

be achieved with the addition of H₂O₂ in the range of 0.1 mM to 10 mM at the initial stage [2]. This presents an opportunity for on-site photocatalytic H₂O₂ generation as an alternative to the additional H₂O₂ supply. However, generating mM-level H₂O₂ under UV light is challenging due to the tendency of UV light to decompose H₂O₂ even at a small dose [12,13]. Achieving these H₂O₂ concentrations necessitates a substantial increase in the H₂O₂ formation rate to surpass its decomposition rate. Previous reports show that the well-established TiO₂ photocatalyst can produce a far low amount of H₂O₂ (20.8 μM/h), which cannot meet the requirement of the UV/H₂O₂ technology [14].

The enhancement of H₂O₂ production by creating O vacancies has been previously studied [15], primarily due to their capability to improve charge separation, as well as the adsorption and activation of O₂. However, oxygen vacancies demonstrate limited improvements in the water oxidation reaction (WOR) to H₂O₂, which is recognized as more difficult than the O₂ reduction pathway. Therefore, the overall H₂O₂ generation from both O₂ reduction and H₂O oxidation will be limited by the latter [16]. Conversely, cation vacancies have exhibited

* Corresponding author at: Key Laboratory of Synthetic and Biological Colloids, Ministry of Education, School of Chemical and Material Engineering, Jiangnan University, Wuxi, Jiangsu 214122, China.

E-mail address: cspan@jiangnan.edu.cn (C. Pan).

<https://doi.org/10.1016/j.apcatb.2024.123854>

Received 15 December 2023; Received in revised form 6 February 2024; Accepted 14 February 2024

Available online 15 February 2024

0926-3373/© 2024 Elsevier B.V. All rights reserved.

positive effects on both the reduction and oxidation processes [17] by tuning the defect energy levels near the valence band of the catalysts and affecting the adsorption configuration and energy of redox intermediates. For example, titanium-vacancy-enriched $\text{Bi}_4\text{Ti}_3\text{O}_{12}$ [18] and V_{Zn} -rich ZnS [19] have shown superior photocatalytic activity to the counterparts without cation vacancies for pollutant oxidation and CO_2 reduction, respectively. The introduction of cation vacancies in UV-responsive photocatalysts may improve the H_2O_2 formation rate [20]. However, the precise influence of cation vacancies on photocatalytic H_2O_2 production has not been comprehensively elucidated.

Hexagonal phase-coated monoclinic BiPO_4 (space group: P21/n) was previously reported [21] to produce H_2O_2 from both H_2O oxidation and O_2 reduction under UV light irradiation. The production rate reaches nearly 200 $\mu\text{M}/\text{h}$, far exceeding that reported for TiO_2 (20.8 $\mu\text{M}/\text{h}$). The high activity results from the selective permeability of hexagonal BiPO_4 coating that can inhibit the decomposition of the produced H_2O_2 by preventing its contact with the active monoclinic photocatalyst surface. However, the coating has a significant UV shielding effect, which would lead to minimum UV light availability for the in-situ H_2O_2 decomposition to generate $\bullet\text{OH}$ radicals for pollutant removal. Consequently, there is a need for further improvement of BiPO_4 to meet in-situ supply for UV/ H_2O_2 degradation.

In this paper, Bi-vacancy-rich monoclinic BiPO_4 nanocrystals (space group: P21/m, V_{Bi} -BIP) are prepared by a high-temperature hydrolysis reaction at 270 °C. The presence of Bi vacancies in V_{Bi} -BIP is studied through spectroscopic and physical characterization methods. The photocatalytic activity on non-sacrificial H_2O_2 production is evaluated and the impact of these vacancies is clarified. The H_2O_2 production rate with this catalyst reaches 26.7 $\text{mM}\cdot\text{g}^{-1}\cdot\text{h}^{-1}$, which is the highest in inorganic photocatalysts without loading cocatalysts. The efficient H_2O_2 production that relates to the strengthening of both O_2 and H_2O adsorption originating from the bare positive charges at Bi-vacancies is demonstrated. Particularly, the improvement of the water oxidation pathway by the presence of surrounding O dangling bonds at Bi-vacancies is illustrated. Furthermore, the UV degradation of antibiotic pollutants utilizing in-situ produced H_2O_2 is compared with traditional UV/ H_2O_2 technology and its long-term performance is tested in a flow cell.

2. Experimental procedures

All chemicals are purchased from Sinopharm Chemical Reagent Co., Ltd (Shanghai, China) and used without further purification. Ultrapure water (18.2 M Ω) is used in all experiments.

2.1. Preparation of Bi-vacancy-rich BiPO_4 nanocrystals (V_{Bi} -BIP)

V_{Bi} -BIP is prepared by a high-temperature hydrolysis method. In a typical procedure, 38 mL oleic acid (OA) and 2 mL bis(2-ethyl-hexyl) phosphate (BEHP) are mixed to form a homogeneous pale yellow solution (Supporting Information Figure S1). Then 5 mmol $\text{Bi}(\text{NO}_3)_3\cdot 5\text{H}_2\text{O}$ is added into the solution to form a suspension with white precipitates. The suspension is stirred in a water bath at 40 °C for 18 h to form a transparent solution. Subsequently, the solution is transferred into a three-necked bottle linked to a Schlenk line. Oxygen and water in the reaction system are removed by evacuating and purging with Ar for three times. The reaction solution is started by heating the solution to 270 °C at a rate of 10 °C/min and kept for 15 min under Ar protection. After that, the solution is cooled down to room temperature naturally. 50 mL of anhydrous ethanol is poured into the reactant solution to form white precipitants. The precipitants are collected by centrifugation at 8000 rpm for 10 min, followed by two washes with ethanol and cyclohexane for each. The final product is dried in a vacuum oven at 60 °C for 2 h.

2.2. Preparation of Bi-refilled V_{Bi} -BIP

150 mg (ca. 0.5 mmol) of the prepared V_{Bi} -BIP and 50 mg $\text{Bi}(\text{NO}_3)_3\cdot 5\text{H}_2\text{O}$ (ca. 0.1 mmol) were dispersed into an HNO_3 aqueous solution (0.1 M) and stirred at room temperature for 24 h. After the reaction, the powders are collected by centrifugation at 8000 rpm for 10 min and washed with ethanol and cyclohexane twice for each. The samples are dried in a vacuum oven at 60 °C.

2.3. Characterizations

The crystal structure of nanocrystals is characterized by a powder X-ray diffraction (XRD) with a Cu K α (1.5418 Å) monochromator at 40 kV and 40 mA. Transmission electron microscopy (TEM, JEOL 2100plus, Japan) is used to characterize the morphology of materials. The spectra of O1s, Bi4f, P2p, and valence band spectra are obtained by X-ray photoelectron spectroscopy (XPS, Axis Supra instrument, Kratos, UK) with Al K α monochromatized radiation ($h\nu=1486.6$ eV, 225 W). The electron paramagnetic resonance (EPR) experiments are carried out on a Bruker EMXplus-6/1 EPR spectrometer. (Center Field: 3505.00 G, Sweep Width: 100 G or 200 G, Power: 6.325 mW, Power Atten: 15.0 dB, Frequency Mon: 9.825444 GHz, Sweep Time: 30.00 s, Mod Amp: 3.000 G, Mod Freq: 100.00 kHz). Fourier-transform infrared (FT-IR) spectra of samples are recorded on a Nicolet iS5 spectrometer (Thermo, USA) with ATR accessories. In-situ IR is performed by a Nicolet iS50 FT-IR spectrometer (Thermo Scientific, USA) equipped with an MCT detector cooled with liquid nitrogen. The Raman spectra are recorded on a lab-made Smart Raman confocal-micro-Raman module (a $\times 100$ objective lens (NA = 0.90) with a backscattering geometry which is obtained from the Institute of Semiconductors, Chinese Academy of Sciences, China) coupled with an iHR550 Raman spectrometer (Horiba, Japan) and a charge-coupled device (CCD) detector. The ultraviolet-visible DRS absorption spectra are performed on a UV-3600 plus ultraviolet-visible (UV-Vis) spectrophotometer (Shimadzu, Japan). The photoluminescence (PL) spectra of all materials are measured by a photoluminescence spectrometer (FS5, Edinburgh, UK). The Rotating Disk Electrode (RDE) and Rotating Ring Disk Electrode (RRDE) measurements are tested using a rotating ring disk electrode instrument (RRDE-3A, Japan) coupled with an electrochemical workstation. (CHI-750E, Chenhua, Shanghai, China). High-performance liquid chromatography (HPLC, Ultimate 3000 RS, Japan) is used to detect the concentration of pollutant solution. The concentration of H_2O_2 and $\bullet\text{OH}$ are measured by the photoluminescence spectrometer. Temperature programmed desorption with mass spectrometry analysis (TPD-MS) profile is tested by a Programmed temperature chemisorption analyzer (BELCAT-II, MicrotracBEL, Japan).

2.4. Photocatalytic production of H_2O_2 for in-situ degradation of pollutants

15 mg sample is dispersed in 30 mL solutions containing pollution (5 ppm) by ultrasonification. UV lamp (254 nm, 18 W) is used for the reaction with a light intensity of 4 mW/cm^2 on the reaction solution.

For the flow-through reaction, BiPO_4 sample is loaded in between two semipermeable membranes. Typically, 500 mg sample is dispersed in ethanol by ultrasonication, and then the suspension is dropped onto the semipermeable membrane. The membrane is dried naturally to form a uniform film. During the reaction, the UV lamp is set into the cold trap, and the membrane is wrapped outside the cold trap. The ciprofloxacin (CIP) solution (5 ppm) is put into the wastewater tank and flowed into the reactor with a pump. The clean water after the reaction is also flowed out the reactor with the pump. The flow rates at the inlet and outlet are both 40 mL/min.

3. Results and Discussion

3.1. Structural characterization of the prepared V_{Bi} -rich BiPO_4

Figs. 1a and 1b show the TEM for the prepared V_{Bi} -BIP nanocrystals. The nanocrystals exhibit an average particle size of 4.2 nm, and clear lattice fringes with 0.352 nm and 0.356 nm, matching well with the (020) and (101) planes (Supporting Information, Fig. S2). The exposed planes are perpendicular to the observed planes, which are the (101) planes of BiPO_4 (space group: P21/m). Moreover, the observed crystalline structure matches well with the inset structural model of (101) planes (magnified image in Fig. 1c), confirming the exposed planes are (101). Note that Fig. 1b shows the contrast of some atomic columns (in white circles) are weaker than others. This might be a result of a lack of Bi^{3+} cations in the prepared BiPO_4 nanocrystals, as reported for Bi_2WO_6 and $\text{Bi}_{24}\text{O}_{31}\text{Br}_{10}$ containing Bi vacancies [22,23].

Fig. 1d and Table S1 (Supporting Information) show the XRD refinement of the prepared V_{Bi} -BIP. The pristine pattern matches well with the fitting line, with the indicators of the fitting goodness, R_{wp} of 7.28%, and χ^2 of 1.82. Similar values have been reported in $\text{Zn}_{1-x}(\text{Li}_{0.5}\text{Bi}_{0.5})_x\text{WO}_4$ [24] and $\text{BiVO}_4/\text{Bi}_{25}\text{VO}_{40}$ [25], indicating our fitting is reasonable. The fitting results show that the prepared BiPO_4 belongs to the space group of P21/m, which is consistent with our TEM observations. The occupation of Bi is 0.962, while that of P is 1.037, confirming the existence of Bi vacancies (ca. 7 mol%) rather than P vacancies. Additionally, the occupation of O is 1.061, 1.051, and 1.044, suggesting O vacancies may barely exist. The ICP-AES (Supporting Information, Table S2) shows that the Bi: P ratio is 0.939:1, which agrees with our fitting results and again confirms the existence of Bi vacancies.

Fig. 1e shows the Raman spectra of V_{Bi} -BIP and bulk BIP (particle size: 500–1500 nm in Supporting Information, Fig. S3). Two sets of peaks located at 1200–300 cm^{-1} and 300–100 cm^{-1} are observed, corresponding to the vibrations of the PO_4 groups and Bi-O vibration in the lattice [26]. V_{Bi} -BIP shows clear negative shifts of the Bi-O vibration

compared to the bulk BIP, indicating the weakening of the Bi-O bond energy. This can be attributed to the existence of Bi vacancies in the lattice [27]. In contrast to Bi-O vibrations, only small shifts are observed for PO_4 , mainly for the ν_2 vibrations (485 cm^{-1} and 352 cm^{-1}), where asymmetric bending occurs with P atoms stationary and O atoms moving. Since Bi^{3+} and PO_4^{3-} are arranged alternately in three dimensions within BiPO_4 (Fig. 1e inset), the presence of Bi vacancies is believed to influence O atoms in neighboring PO_4^{3-} cations, resulting in the observed peak shift. The FTIR and ^{31}P -ssNMR results (Supporting Information, Fig. S4 and S5) also show the neighboring PO_4^{3-} cations are influenced by the presence of Bi vacancies, supporting the Raman observations.

Fig. 1f shows the EPR spectra of V_{Bi} -BIP, Bi-refilled V_{Bi} -BIP (particle size: 4.5 nm in Supporting Information, Fig. S6), and bulk BIP. The spectra show a symmetrical signal located at $g = 1.998$. This peak originates from the unpaired electrons of the atoms surrounding vacancies [12]. On the contrary, negligible signals are found for bulk BIP, indicating almost no vacancies exist in bulk material. To determine whether the signal originates from Bi vacancies or O vacancies, Bi^{3+} cations were refilled into the vacancies of V_{Bi} -BIP. ICP results (Supporting Information, Table S2) show the Bi: P ratio of Bi-refilled V_{Bi} -BIP increases from 0.939:1–0.986:1, indicating that 77% of the vacancies are now refilled by Bi^{3+} . For the Bi-refilled sample, the EPR signals decrease to one-ninth relative to those of the unfilled one. Even if O vacancies exist, Bi^{3+} cations prefer to refill in the Bi vacancies rather than the O vacancies due to the size and charge differences, the decrease in EPR signal for the Bi-refilled V_{Bi} -BIP indicates the observed EPR signals belong to the Bi vacancies. Additionally, the result of XPS also proves that most of the vacancies are now refilled by Bi^{3+} (Supporting Information Figure S7).

The $\text{Bi}4f$ XPS narrow scan (Supporting Information, Fig. S8) for BIP shows a pair of peaks located at the binding energy of 159.9 eV and 165.2 eV, which can be assigned as $4f_{7/2}$ and $4f_{5/2}$ states of the Bi^{3+} in BiPO_4 , respectively [28]. While for the V_{Bi} -BIP sample, ca. 0.1 eV positive shifts are observed. This phenomenon could be attributed to the

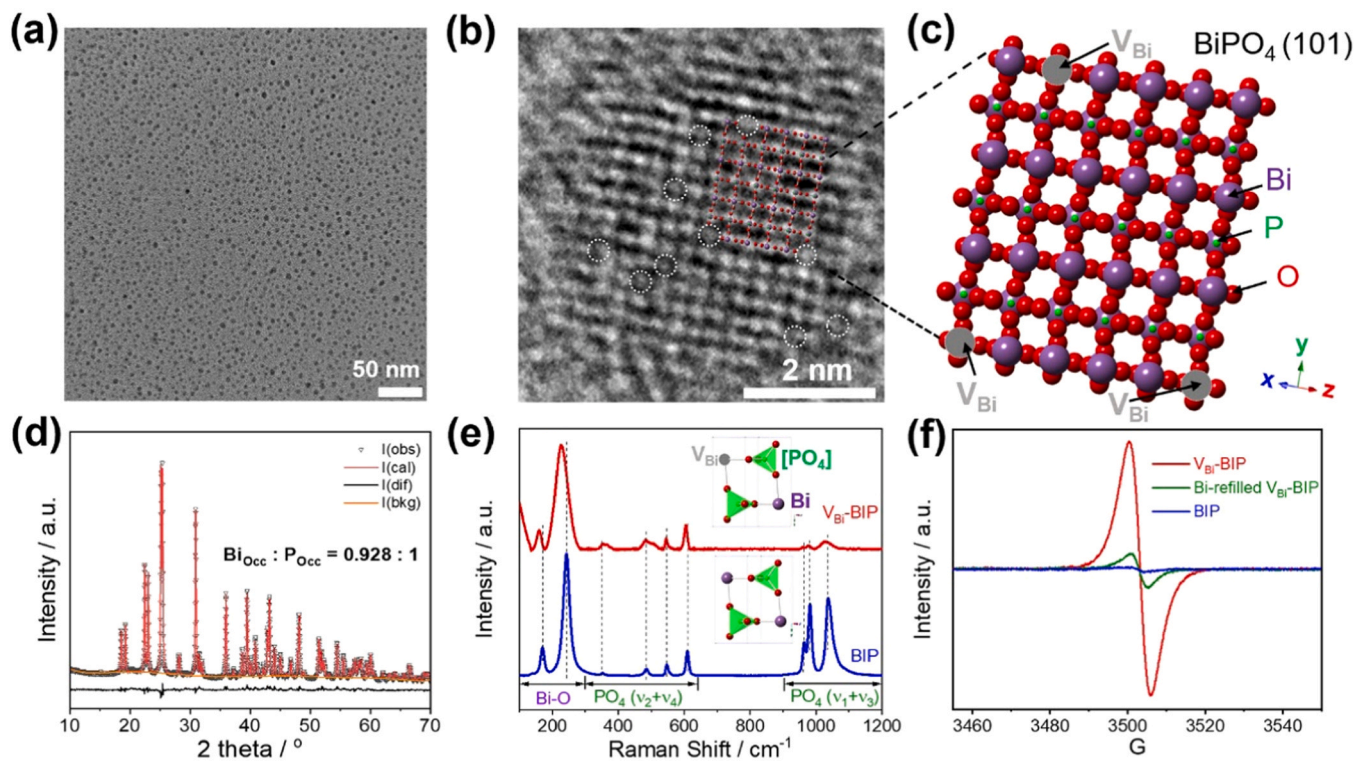


Fig. 1. Physical characterization of V_{Bi} -BIP nanocrystals. (a) TEM and (b) HRTEM of V_{Bi} -BIP. (c) Structural schematics of Bi-vacancies on the (101) surface of BIP nanocrystals. (d) XRD refinement of V_{Bi} -BIP nanocrystals. Inset is the ratio of Bi and P occupancies obtained from XRD refinement. (e) Raman spectra of V_{Bi} -BIP nanocrystals and bulk BIP. (f) EPR spectra for V_{Bi} -BIP nanocrystals, Bi-refilled V_{Bi} -BIP nanocrystals, and bulk BIP.

formation of Bi vacancies [29,30]. Besides, the P2p and O1s XPS narrow scans (Supporting Information, Fig. S8c and S8d) also show changes that are consistent with the presence of Bi vacancies.

The calculated total density of states (TDOS) plots and measured XPS valence band spectra of V_{Bi} -BIP and bulk BIP (Supporting Information, Fig. S8e and S8f) indicate that the energy level of Bi vacancies is located at the valence band maximum. The UV-Vis DRS results reveal that the band gap of BIP is 4.43 eV and the Urbach bandgap originating from the defects is 3.72 eV. Combining the UPS results, the valence band potential is determined to be 3.30 V vs. NHE, while the conduction band edge is -1.13 V [31,32]. This is also proven by the valence band results calculated from Mott-Schottky (MS) curves and bandgap (Supporting Information, Fig. S9). Both the valence band and conduction band edge potentials exceed the O_2 reduction and H_2O oxidation potentials necessary for H_2O_2 production, indicating the potential dual pathways of H_2O_2 production as we previously reported for the $BiPO_4$ material [21].

3.2. Highly efficient H_2O_2 production on V_{Bi} -rich $BiPO_4$ photocatalysts

Fig. 2a shows the H_2O_2 production from H_2O and O_2 on V_{Bi} -BIP, Bi-refilled V_{Bi} -BIP, and bulk BIP. For V_{Bi} -BIP, H_2O_2 concentration reaches $56.61 \text{ mM} \cdot \text{g}^{-1}$ after 3 h irradiation, while only negligible H_2O_2 is produced on bulk BIP. Additionally, the H_2O_2 production in the O_2 -free system as shown in Fig. S10, the H_2O_2 accumulation is only 1/35 of that in O_2 atmosphere. This is due to the fact that the photogenerated

electrons are not consumed as in the O_2 atmosphere through the ORR, leading to the increase of the recombination rate for electrons and holes, and the decrease of H_2O_2 generation activity. To exclude the influence of surface area on activity, Bi-refilled V_{Bi} -BIP with the same nanocrystal structure is tested and produces $8.67 \text{ mM} \cdot \text{g}^{-1}$ H_2O_2 after 3 h irradiation. The activity of the V_{Bi} -BIP is 6.5 times that of the Bi-refilled V_{Bi} -BIP, confirming that the activity should be attributed to Bi vacancies rather than the surface area since the specific surface areas of the two samples are relatively similar (Figure S11). H_2O_2 production facilitated by Bi vacancies is also confirmed by evaluating the O_2 reduction and H_2O oxidation half reaction with IPA and $Na_2S_2O_8$ as sacrificial reagents, respectively (Supporting Information, Fig. S12).

Fig. 2b shows the stability of the activity of V_{Bi} -BIP. After 10 cycles of reactions (30 h total), activity decay is negligible. The EPR spectra before and after UV irradiation (Supporting Information, Fig. S13) illustrate the Bi vacancies are stable in the V_{Bi} -BIP structure during H_2O_2 production. Besides, XRD (Supporting Information, Fig. S14) and FTIR (Supporting Information, Fig. S15) spectra exhibit negligible changes after 10 reaction cycles, confirming the catalyst is stable in both crystal and surface structures.

Fig. 2c shows the apparent quantum yields (AQY) and energy conversion efficiency (ECE) change with reaction time. AQY and ECE peaked at 43.4% and 10.7% respectively. Both the AQY and ECE slightly decrease to 35% and 8.5% after 3 h reaction. This decrease could potentially be attributed to the accumulation of H_2O_2 , which is known to exhibit an elevated decomposition rate under UV irradiation with

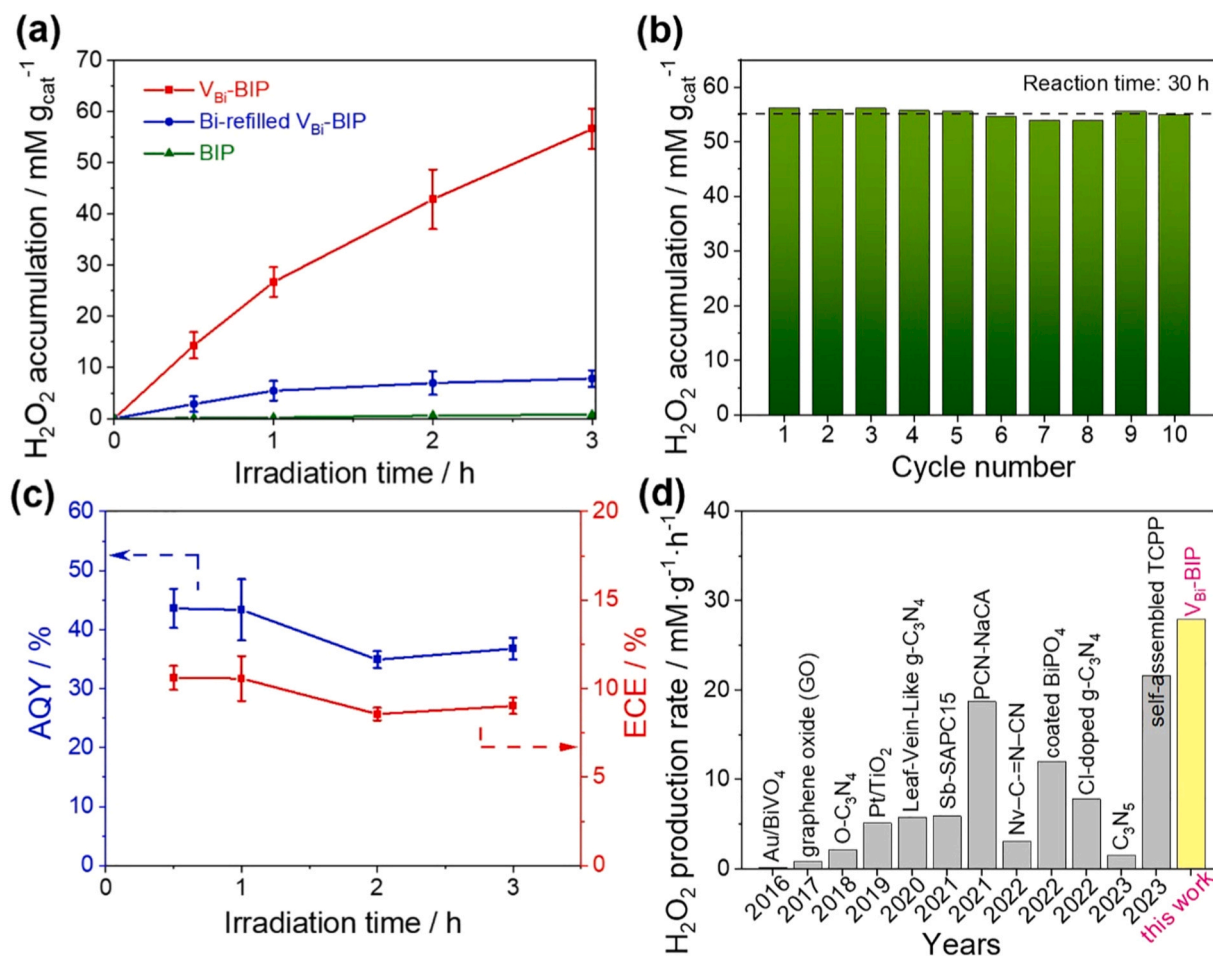


Fig. 2. H_2O_2 generation on V_{Bi} -BIP from only H_2O and O_2 . (a) H_2O_2 production curves on V_{Bi} -BIP nanocrystals, Bi-refilled V_{Bi} -BIP nanocrystals, and bulk BIP. 18 W UV lamp, 30 mL H_2O , 5 mg cat.; (b) The stability test of V_{Bi} -BIP photocatalysts. 18 W UV lamp, 30 mL solvent, 5 mg cat.; (c) The change of AQY and ECE during the H_2O_2 generation. 18 W UV lamp with a 254 ± 10 nm bandpass filter, 30 mL solvent, 45 mg cat.; (d) Activity comparison between V_{Bi} -BIP and other reported photocatalysts [21,34–44].

increasing concentrations. Consequently, this might hinder further net accumulation [33].

Fig. 2d and Table S3 (Supporting Information) compare the photocatalytic activity of V_{Bi} -BiP with other representative photocatalysts for H_2O_2 generation solely from H_2O and O_2 [21,34–44]. The H_2O_2 production rate on V_{Bi} -BiP is $26.7 \text{ mM} \cdot \text{g}^{-1} \cdot \text{h}^{-1}$, which is nearly 2.3 times higher than the hexagonal phase coated monoclinic $BiPO_4$ nanorods reported by our group before ($12.0 \text{ mM} \cdot \text{g}^{-1} \cdot \text{h}^{-1}$) [21]. The activity also exceeds typical inorganic single-component or composite photocatalysts that enable stable H_2O_2 production (0.13 – $18.7 \text{ mM} \cdot \text{g}^{-1} \cdot \text{h}^{-1}$) [34–43]. The activity of V_{Bi} -BiP is also exceeds that of recently reported high-active SA-TCPP ($23.0 \text{ mM} \cdot \text{g}^{-1} \cdot \text{h}^{-1}$) [44].

Next, we investigate the origin of the high H_2O_2 production activity on V_{Bi} -BiP. Fig. 3a shows the RRDE measurements for V_{Bi} -BiP to determine the charge transfer number for the water oxidation reaction during H_2O_2 production. The reported $BiPO_4$ without Bi vacancies is also measured as a control. The average number of charge transfer (n) is measured as 2.58 for WOR to form H_2O_2 . In literature, n close to 2 indicates that a one-step two-charge transfer governs the H_2O_2 generation reaction in this work [42]. On the contrary, the reported $BiPO_4$ [21] exhibits two-step one-charge transfer ($n = 1.78$). The difference in charge transfer number may be attributed to the presence of Bi vacancies. The one-step two-electron transfer is also confirmed by EPR measurement (Supporting Information, Fig. S16), where no signals for hydroxyl radicals, intermediates in a two-step one-electron transfer mechanism, are detected. The data mentioned above show that the presence of Bi vacancies can benefit the WOR to H_2O_2 by promoting a one-step two-electron transfer mechanism that inherently has high selectivity and rapid reaction rate [45,46].

The change of the charge transfer pathway may be partly due to the enhancement of H_2O adsorption onto Bi vacancies as revealed by the

TPD results and DFT calculations (adsorption energies of H_2O : -2.1 eV on V_{Bi} -BiP and -0.3 eV on BiP) in Fig. S17–S19 (Supporting Information). This is because the presence of Bi vacancies results in a positively charged environment, leading to stronger attraction forces with H_2O molecules, while the adsorption of H_2O on Bi atoms in the $BiPO_4$ without Bi vacancies will be reduced by the repulsion force of 6 s^2 lonely pairs. Such an effect may also strengthen O_2 adsorption, enhance the O_2 reduction to H_2O_2 and improve the overall H_2O_2 generation efficiency as demonstrated by the EPR, TPD, DFT, and RDE results in Fig. S16–S21 (Supporting Information).

3.3. Thermodynamically favored lattice oxygen-involved water oxidation pathway induced by Bi-vacancies enhancing the H_2O_2 production

Next, the origin of the one-step two-charge transfer due to the existence of Bi vacancy is elucidated. Fig. 3b shows the in-situ IR spectra for H_2O_2 production on V_{Bi} -BiP. The spectrum is recorded every 10 min and the data at 0 min is employed as a control. During the light on, two peaks at 1431 cm^{-1} and 1115 cm^{-1} emerge and become stronger, while the two peaks' intensities gradually decay when the light is turned off. The two peaks are assigned to *OH adsorbed on phosphate anions and *OOH , respectively, according to previous reports [47]. The IR results confirm that the presence of Bi vacancies benefits the generation of adsorbed *OH and *OOH rather than free $\bullet O_2$ and $\bullet OH$ in solution, and thus, leads to the one-step two-charge transfer. Note that the adsorbed *OH peak is located at a lower wavenumber compared to when *OH binds with metal cations (1600 cm^{-1} – 1700 cm^{-1}). This suggests that *OH may absorb on PO_4 , where a conjugation effect occurs, resulting in the FTIR peak shifting to a low wavenumber [48].

Fig. 3c shows the in-situ Raman spectra for V_{Bi} -rich $BiPO_4$ and Bi-refilled V_{Bi} - $BiPO_4$ on light and in the dark during H_2O_2 generation.

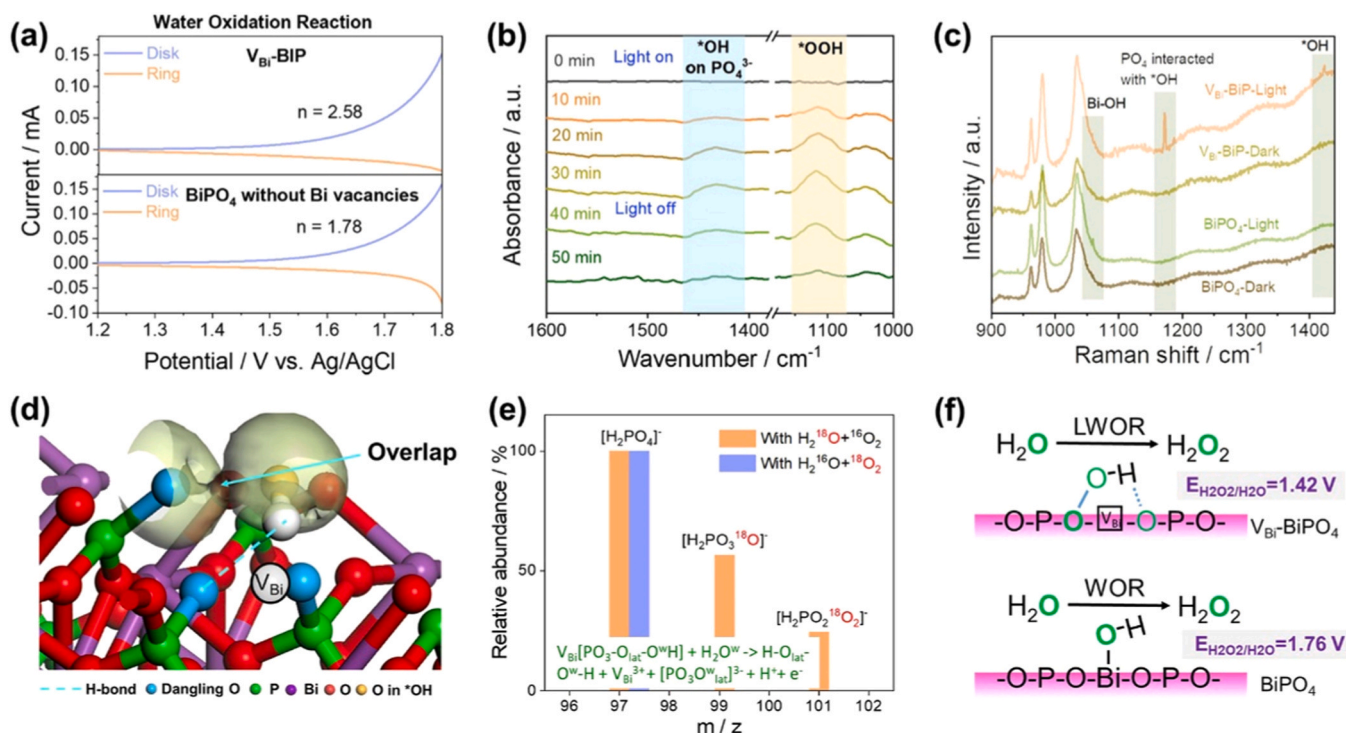


Fig. 3. Lattice oxygen-involved water oxidation reaction to H_2O_2 on V_{Bi} -BiP. (a) RRDE voltammograms for H_2O oxidation on V_{Bi} -BiP and $BiPO_4$ without Bi vacancies (prepared according to Ref. 18); Electrolyte: 0.1 M phosphate buffer solution (pH 7), Scan rate: $10 \text{ mV} \cdot \text{s}^{-1}$, Rotary speed: 1600 rpm, Ar-saturated solution and a ring potential of 0 V vs. Ag/AgCl for WOR; (b) In-situ IR spectra for V_{Bi} -BiP during the H_2O_2 production; (c) In-situ Raman spectra for V_{Bi} - $BiPO_4$ and Bi-refilled V_{Bi} - $BiPO_4$ on light (40 min) and in dark, respectively, during H_2O_2 generation. (d) Electron density difference between the adsorbed *OH and dangling O atoms surrounding Bi vacancies. The pale yellow regions represent electron accumulation area, and the isosurface value is $0.01 \text{ e}/\text{Bohr}^3$. (e) LC-TOF-MS (ESI) of V_{Bi} -BiP after 3 h reaction in $H_2^{18}O$ – $^{16}O_2$ and $H_2^{16}O$ – $^{18}O_2$. (f) Schematics for lattice oxygen-involved water oxidation reaction (LWOR) to H_2O_2 on V_{Bi14} - $BiPO_4$, and water oxidation reaction (WOR) to H_2O_2 on $BiPO_4$.

For Bi-refilled V_{Bi} -BiPO₄, a peak at 1050 cm⁻¹ emerges after irradiation, which can be attributed to the presence of Bi-OH bonds [49]. For V_{Bi} -rich BiPO₄, two new peaks appear after irradiation, located at 1173 cm⁻¹ and 1420 cm⁻¹. These peaks are associated with the stretching of PO₄ units interacting with adsorbed *OH and the bending of *O-H interactions with PO₄, respectively [50–52]. The Raman results suggest in the absence of Bi-vacancies, *OH will interact with Bi³⁺, while in the presence of Bi-vacancies, the adsorbed *OH may interact with PO₄, which coincides with the in-situ FTIR results. Note that Bi vacancies are surrounded by a substantial number of PO₄ units with dangling O atoms. The dangling O atoms may tend to interact with *OH. The electron charge difference between the adsorbed *OH and dangling O atoms (Fig. 3d) exhibits a clear overlap, providing further confirmation of such interactions.

Furthermore, LC-MS analysis reveals that the ¹⁸O in H₂¹⁸O is incorporated into lattice PO₄³⁻ anions, replacing ¹⁶O, while with ¹⁸O₂, this substitution does not occur (Fig. 3e). This implies the lattice O participates in the WOR, but not in the ORR. Control experiments show that without Bi vacancies and without irradiation, ¹⁶O in lattice PO₄³⁻ anions are not substituted by ¹⁸O on Bi-refilled V_{Bi} -BIP after reacting with H₂¹⁸O (Supporting Information, Fig. S22 and S23). Additionally, FTIR peaks for PO₄³⁻ shift to low wavenumbers after reaction with H₂¹⁸O, confirming the existence of ¹⁸O-substituted PO₄³⁻ in the WOR. Conversely, after reacting

with ¹⁸O₂, the PO₄³⁻ peaks remain unchanged, indicating lattice O doesn't participate in the ORR (Supporting Information, Fig. S24). Both in-situ FTIR and Raman results demonstrate that the dangling O atoms surrounding the Bi vacancies will interact with the adsorbed *OH. This may facilitate the subsequent formation of -O_{lat}-O_w-H groups, which easily exchange with OH⁻ anions from H₂O, leading to the formation of [PO₃-O_w]³⁻ groups during the water oxidation process and detected by the LC-MS.

This lattice O-involved water oxidation reaction (LWOR) has been reported in certain 4e⁻ O₂ evolution reactions and is thermodynamically favored over conventional water oxidation [53]. In our case, we have calculated that the potential required for H₂O₂ generation through LWOR is 1.42 V, which is 0.34 V lower than that for typical water oxidation reaction to H₂O₂ (1.76 V) (see Supporting Information, Note S1). Therefore, the high activity observed on V_{Bi} -BIP may be attributed not only to the enhanced adsorption of O₂ and H₂O on the vacancies, but also to the thermodynamic preference of LWOR facilitated by the presence of Bi-vacancy structures. Moreover, the calculated Gibbs free energy for the *OH formation during water oxidation on V_{Bi} -BIP is 0.7 eV lower than that on BIP, and for *OOH formation during O₂ reduction on V_{Bi} -BIP, the Gibbs free energy is reduced by 0.3 eV (Supporting Information, Fig. S25). The large decrease in the *OH formation energy support the conclusion that dangling oxygen atoms surrounding

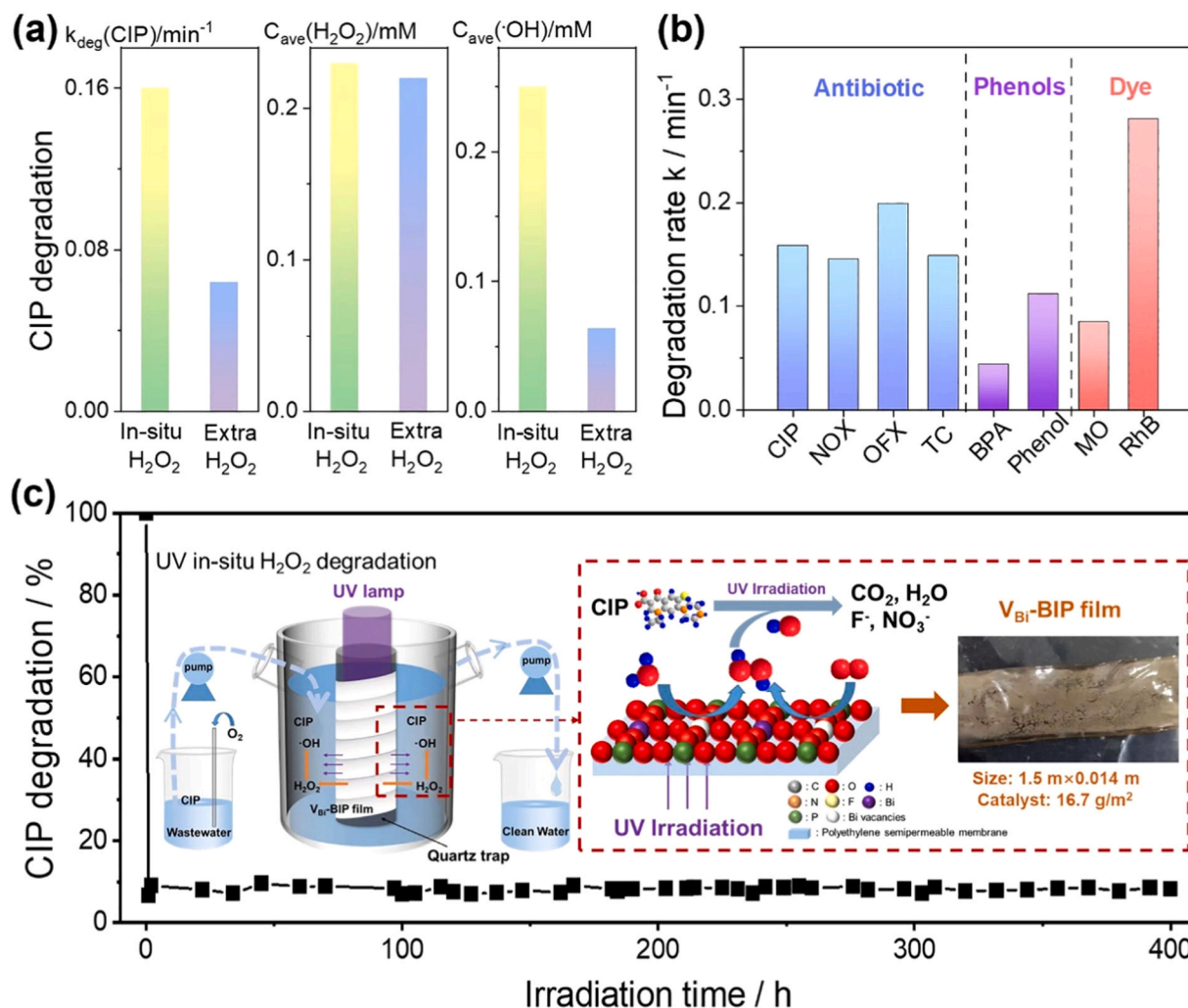


Fig. 4. Degradation performance with in-situ photocatalytically produced H₂O₂. (a) CIP degradation by in-situ H₂O₂ and extra added H₂O₂ under UV light and the average H₂O₂ and •OH concentration in each method. Solution: 30 mL, CIP: 5 ppm, Cat.: 0.5 g·L⁻¹, Light source: 18 W UV lamp. Extra H₂O₂ concentration at 0 min: 1 mM; (b) Photodegradation of various organic pollutants with in-situ H₂O₂ on V_{Bi} -BIP; (c) CIP degradation in a flow reactor with in-situ H₂O₂ generated on V_{Bi} -BIP film cast between two polyethylene semipermeable membranes. Light source: 36 W UV lamp, Catalyst loading: 0.167 g·cm⁻², Flow rate: 40 mL·min⁻¹.

Bi vacancies play a pivotal role in promoting water oxidation, which, in turn, facilitates H_2O_2 generation (Fig. 3f).

3.4. Efficient H_2O_2 generation on $\text{V}_{\text{Bi}}\text{-BiPO}_4$ enabling a stable on-site supply in UV/ H_2O_2 technology with an excellent removal efficiency

Encouraged by the impressive H_2O_2 production achieved with $\text{V}_{\text{Bi}}\text{-BIP}$, the generated H_2O_2 is harnessed for in-situ UV/ H_2O_2 degradation for organic pollutants. As a representative, CIP is chosen because it is one of the most commonly detected antibiotic contaminants in natural water bodies [54].

Fig. 4a and Fig. S26 (Supporting Information) display the CIP removal activity, and the average concentrations of H_2O_2 and the generated $\bullet\text{OH}$ during the in-situ H_2O_2 degradation process. The results show that 92% of CIP can be removed within 12 min, and the concentrations of H_2O_2 and $\bullet\text{OH}$ remain relatively constant at 0.23 mM and 0.15 mM. TOC removal reaches 91% after irradiation with UV irradiation for 1 h (Supporting Information, Fig. S27). As a reference, the average $\bullet\text{OH}$ and H_2O_2 concentrations are measured during the CIP degradation with the traditional UV/ H_2O_2 method (Fig. 4a and Supporting Information, Fig. S28). With the extra addition of 1 mM H_2O_2 , the average $\bullet\text{OH}$ concentration and H_2O_2 concentration are 0.064 mM and 0.22 mM. H_2O_2 decomposes quickly at the initial stage and cannot effectively form $\bullet\text{OH}$ radicals during the whole degradation (Supporting Information, Fig. S28). The large decrease for $\bullet\text{OH}$ concentration is observed in the latter system, responsible for 2.5 times enhancement of the CIP degradation rate by in-situ H_2O_2 method relative to the conventional extra H_2O_2 method. To exclude the degradation of pollutants by the photocatalyst directly in the current in-situ system, MnO_2 is added to decompose the produced H_2O_2 into O_2 (Supporting Information, Fig. S29). In this case, the net degradation rate constant is 0.006 min^{-1} , which is less than one-twentieth of that of the in-situ system (0.16 min^{-1}), indicating the pollutants are mainly degraded by in-situ produced H_2O_2 rather than by the photocatalysts directly. This is presumably because the high concentrations of H_2O (55.6 M) and O_2 (0.25 mM, at 25°C , 1 atm) [55] in the solution far exceeding the pollutant concentration (0.015 mM) result in a faster H_2O_2 generation relative to the pollutant degradation on the photocatalyst.

In order to verify sustainability and stability of $\text{V}_{\text{Bi}}\text{-BIP}$, the performance was tested at different pH values (pH=3,5,7,9,11), in the presence of inorganic ions (Na^+ , Ca^{2+} , Mg^{2+} , Cl^- , CO_3^{2-} , SO_4^{2-}) and NOM (Supporting Information Figure S30). In our case, $\text{V}_{\text{Bi}}\text{-BIP}$ exhibits excellent performance in degrading CIP across a wide pH range and can remove over 80% of CIP after irradiation for 12 min. Moreover, the degradation of CIP by $\text{V}_{\text{Bi}}\text{-BIP}$ is minimally affected by different inorganic ions and low concentrations of NOM, suggesting that the utilization of $\text{V}_{\text{Bi}}\text{-BIP}$ for the in-situ photocatalytic degradation of CIP is sustainable and stable. Additionally, $\text{V}_{\text{Bi}}\text{-BIP}$ exhibited comparable degradation performance in tap water (0.17 min^{-1}) but decreased by 35% in secondary treated wastewater (SWW) (0.11 min^{-1}). The decrease can be attributed to the higher concentrations of various mineral species and organic matter present in SWW compared to other water sources [56].

The degradation selectivity is further evaluated using in-situ produced H_2O_2 to degrade additional pollutants (Fig. 4b). The results show that similar to CIP, tetracycline (TC) (which is also hydrophobic) exhibits a similar degradation rate constant of 0.15 min^{-1} . On the other hand, hydrophilic antibiotics like norfloxacin (NOX) and ofloxacin (OFX) show a similar degradation rate to CIP, at 0.14 min^{-1} and 0.20 min^{-1} respectively. Other than antibiotics, pollutants commonly found in water like dyes and phenols (e.g. rhodamine B (RhB), methyl orange (MO), bisphenol A (BPA), phenol) are also subjected to testing. These pollutants also exhibited rapid degradation in the in-situ H_2O_2 production system. The degradation rate constants on various pollutants are somewhat different, which is likely caused by the difference in the capability of $\bullet\text{OH}$ to degrade the various pollutants (Supporting

Information, Fig. S32). Note that although the degradation rates for different pollutants (i.e. CIP, BPA, and RhB) are different, the H_2O_2 concentration (ca. 0.22 mM) during the degradation is similar, indicating the observed H_2O_2 mainly due to the generation from H_2O and O_2 on $\text{V}_{\text{Bi}}\text{-BIP}$ (Supporting Information, Fig. S33).

The degradation efficiency of the in-situ H_2O_2 production system is further evaluated using a flow reactor containing a $\text{V}_{\text{Bi}}\text{-BIP}$ film cast between two Polyethylene semipermeable membranes. The mobile phase is a continuously flowing CIP solution at a concentration of 5 ppm. Fig. 4c and Fig. S34 (Supporting Information) shows the setup (inset), the photo of the reactor and results of the test that was carried out for 400 h. Approximately 92% of CIP is degraded during the reaction time without obvious activity decay. H_2O_2 concentration is also sampled at 10 h, 200 h, and 400 h to be 147.4 μM , 142.6 μM , and 134.2 μM , respectively, demonstrating the stable and continuous capability of in-situ H_2O_2 generation during pollutant degradation. For the flow reactor, the energy cost per unit order (EE/O, the electric or light energy required to degrade a target contaminant by 1 order of magnitude in a unit volume of contaminated water) is calculated, and values of $\sim <0.5\text{--}10 \text{ kWh/m}^3$ are considered competitive for drinking water applications [57,58]. The EE/O in our in-situ H_2O_2 degradation system is 0.58 kWh/m^3 , which saves more energy required for a traditional UV/ H_2O_2 system, whose EE/O is $0.9\text{--}9.1 \text{ kWh/m}^3$ [59].

4. Conclusion

In summary, Bi-vacancy-rich BiPO_4 nanocrystals are prepared with a high-temperature hydrolysis method. The prepared nanocrystals have a particle size of $4.5 \pm 2 \text{ nm}$, and the concentration of Bi-vacancies is ca. 7 mol%. The H_2O_2 production rate, AQY, and ECE reach $26.7 \text{ mM}\cdot\text{g}^{-1}\cdot\text{h}^{-1}$, 43.4%, and 10.7%, at $254 \pm 10 \text{ nm}$, respectively. The presence of Bi vacancies enhances the adsorption of H_2O via the formation of bare positive charge, which facilitates the subsequent charge transfer. More importantly, the dangling O atoms surrounding the vacancies have been demonstrated to aid in the dissociation of adsorbed H_2O , thus participate in the WOR process to form H_2O_2 . The in-situ produced H_2O_2 is highly effective and stable in degrading organic pollutants, showing a 92% removal for 400 h with a flow rate of 2.4 L/h. This work provides new insights into the future development of photocatalysts for the highly efficient H_2O_2 generation from H_2O and O_2 and in-situ degradation of pollutants.

CRediT authorship contribution statement

Chen Chaofeng: Writing – original draft, Software, Methodology, Data curation, Conceptualization. **Pan Chengsi:** Writing – review & editing, Supervision, Methodology, Investigation, Conceptualization. **Sun Hao:** Data curation. **Xu Jing:** Methodology, Formal analysis. **Wang Chen:** Writing – review & editing, Supervision. **Zhang Yaning:** Data curation. **Zhang Ying:** Visualization, Investigation. **Lou Yang:** Methodology, Investigation. **Zhu Yongfa:** Writing – review & editing, Methodology, Investigation.

Declaration of Competing Interest

The authors declare that they have no known competing financial interests or personal relationships that could have appeared to influence the work reported in this paper.

Data Availability

Data will be made available on request.

Acknowledgments

This work was supported by the National Natural Science Foundation

of China (22172065, 21908079, 21676123, 21902009, 21707052, U21A20326), Special Fund Project of Jiangsu Province for Scientific and Technological Innovation in Carbon Peaking and Carbon Neutrality (BK20220023), National Key R&D Program of China (2021YFB3501900), Jiangsu Specially-Appointed Professor (1046010241211400). The authors also thank the Central Laboratory, School of Chemical and Material Engineering, Jiangnan University.

Appendix A. Supporting information

Supplementary data associated with this article can be found in the online version at doi:10.1016/j.apcatb.2024.123854.

References

- [1] W.C. Schumb, Hydrogen Peroxide, in: C.N. Satterfield, R.L. Wentworth (Eds.), ACS Monograph No. 128, Reinhold Publishing, Co., New York, 1955.
- [2] J.C. Kruihof, P.C. Kamp, B.J. Martijn, UV/H₂O₂ treatment: a practical solution for organic contaminant control and primary disinfection, *Ozone Sci. Eng.* 29 (2007) 273–280.
- [3] J.R. Bolton, J.E. Valladares, J.P. Zanin, W.J. Cooper, M.G. Nickelsen, D.C. Kajdi, T. D. Waite, C.N. Kurucz, Figures-of-merit for advanced oxidation technologies: a comparison of homogeneous UV/H₂O₂, heterogeneous UV/TiO₂ and electron beam processes, *J. Adv. Oxid. Technol.* 3 (1998) 174–181.
- [4] Y. Huang, M. Kong, S. Coffin, K.H. Cochran, D.C. Westerman, D. Schlenk, S. D. Richardson, L. Lei, D.D. Dionysiou, Degradation of contaminants of emerging concern by UV/H₂O₂ for water reuse: kinetics, mechanisms, and cytotoxicity analysis, *Water Res.* 174 (2020) 115587.
- [5] W.H. Glaze, J.-W. Kang, D.H. Chapin, The chemistry of water treatment processes involving ozone, hydrogen peroxide and ultraviolet radiation, *Ozone Sci. Eng.* 9 (1987) 335–352.
- [6] M. Li, M. Sun, H. Dong, J. Zhang, Y. Su, Z. Qiang, Enhancement of micropollutant degradation in UV/H₂O₂ process via iron-containing coagulants, *Water Res.* 172 (2020) 115497.
- [7] P. Vitale, P.B. Ramos, V. Colasurdo, M.I. Delletesse, G.P. Barreto, Degradation of printing ink effluent and industrial predesign by UV/H₂O₂ treatment: a kinetic study, *Clean. Waste Syst.* 5 (2023) 100106.
- [8] M.S. Kim, C. Lee, J.H. Kim, Occurrence of unknown reactive species in UV/H₂O₂ system leading to false interpretation of hydroxyl radical probe reactions, *Water Res.* 201 (2021) 117338.
- [9] J. Zhang, Q. Zheng, C. Chen, X. Zhang, X. Guo, M. Long, Sequencing batch photocatalytic H₂O₂ production over a magnetic resorcinol–formaldehyde polymer for on-site water purification by UV light irradiation, *Environ. Sci. Adv.* 2 (2023) 98–106.
- [10] K. Guo, Z. Wu, S. Yan, B. Yao, W. Song, Z. Hua, X. Zhang, X. Kong, X. Li, J. Fang, Comparison of the UV/chlorine and UV/H₂O₂ processes in the degradation of PPCPs in simulated drinking water and wastewater: Kinetics, radical mechanism and energy requirements, *Water Res.* 147 (2018) 184–194.
- [11] Y. Chen, Y. Li, N. Luo, W. Shang, S. Shi, H. Li, Y. Liang, A. Zhou, Kinetic comparison of photocatalysis with H₂O₂-free photo-Fenton process on BiVO₄ and the effective antibiotic degradation, *Chem. Eng. J.* 429 (2022) 132577.
- [12] Y. Sun, L. Han, P. Strasser, A comparative perspective of electrochemical and photochemical approaches for catalytic H₂O₂ production, *Chem. Soc. Rev.* 49 (2020) 6605–6631.
- [13] F. Cataldo, Hydrogen peroxide photolysis with different UV light sources including a new UV-LED light source, *New Front. Chem.* 23 (2014) 99–110.
- [14] D. Tsukamoto, A. Shiro, Y. Shiraishi, Y. Sugano, S. Ichikawa, S. Tanaka, T. Hirai, Photocatalytic H₂O₂ production from ethanol/O₂ system using TiO₂ loaded with Au–Ag bimetallic alloy nanoparticles, *ACS Catal.* 2 (2012) 599–603.
- [15] R. Gao, L. Pan, Z. Li, C. Shi, Y. Yao, X. Zhang, J.J. Zou, Engineering facets and oxygen vacancies over hematite single crystal for intensified electrocatalytic H₂O₂ production, *Adv. Funct. Mater.* 30 (2020) 1910539.
- [16] C. Feng, J. Luo, C. Chen, S. Zuo, Y. Ren, Cooperative tungsten centers in polymeric carbon nitride for efficient overall photosynthesis of hydrogen peroxide, *Energy Environ. Sci.* (2024). DOI: 10.1039/d3ee03032f.
- [17] L. Cao, B.W. Zhang, S. Zhao, Cation-tuning engineering on metal oxides for oxygen electrocatalysis, *Chem. Eur. J.* 29 (2023) e202202000.
- [18] D. Zhang, Y. Li, P. Wang, J. Qu, S. Zhan, Y. Li, Regulating spin polarization through cationic vacancy defects in Bi₄Ti₃O₁₂ for enhanced molecular oxygen activation, *Angew. Chem. Int. Ed.* 62 (2023) e202303807.
- [19] H. Pang, X. Meng, P. Li, K. Chang, W. Zhou, X. Wang, X. Zhang, W. Jevasuwan, N. Fukata, D. Wang, J. Ye, Cation vacancy-initiated CO₂ photoreduction over ZnS for efficient formate production, *ACS Energy Lett.* 4 (2019) 1387–1393.
- [20] F. Xue, C. Zhang, H. Peng, L. Sun, X. Yan, F. Liu, W. Wu, M. Liu, L. Liu, Z. Hu, C. Kao, T. Chan, Y. Xu, X. Huang, Modulating charge centers and vacancies in P-CoNi loaded phosphorus-doped ZnIn₂S₄ nanosheets for H₂ and H₂O₂ photosynthesis from pure water, *Nano Energy* 117 (2023) 108902.
- [21] C. Pan, G. Bian, Y. Zhang, Y. Lou, Y. Zhang, Y. Dong, J. Xu, Y. Zhu, Efficient and stable H₂O₂ production from H₂O and O₂ on BiPO₄ photocatalyst, *Appl. Catal. B Environ.* 316 (2022) 121675.
- [22] Z. Kang, E. Lin, N. Qin, J. Wu, D. Bao, Bismuth vacancy-mediated quantum dot precipitation to trigger efficient piezocatalytic activity of Bi₂WO₆ nanosheets, *ACS Appl. Mater. Interfaces* 14 (2022) 11375–11387.
- [23] Y. Li, K. Xu, H. Hu, L. Jia, Y. Zhang, C. Zhuoga, P. Yang, X. Tan, W. Guo, W. Hao, T. Yu, J. Ye, Bi vacancy simultaneous manipulation of bulk adsorption and carrier utilization to replenish the mechanism of Cr(VI) photoreduction at universal pH, *Chem. Eng. J.* 450 (2022) 138106.
- [24] Q. Zhang, H. Su, H. Zhang, X. Tang, Bond, vibration and microwave dielectric characteristics of Zn_{1-x}(Li_{0.5}Bi_{0.5})_xWO₄ ceramics with low temperature sintering, *J. Mater.* 8 (2022) 392–400.
- [25] X. Liu, Y. Liu, T. Liu, Y. Jia, H. Deng, W. Wang, F. Zhang, Alkali-mediated dissolution-recrystallization strategy for in situ construction of a BiVO₄/Bi₂₅VO₄₀ heterojunction with promoted interfacial charge transfer: Formation mechanism and photocatalytic tetracycline degradation studies, *Chem. Eng. J.* 431 (2022) 134181.
- [26] A.B. Azzam, S.M. El-Sheikh, R.A. Geioushy, B.A. Salah, F.M. El-Dars, Facile fabrication of a novel BiPO₄ phase junction with enhanced photocatalytic performance towards aniline blue degradation, *A. S. Helal RSC Adv.* 9 (2019) 17246–17253.
- [27] J. Di, C. Chen, C. Zhu, M. Ji, J. Xia, C. Yan, W. Hao, S. Li, H. Li, Z. Liu, Bismuth vacancy mediated single unit cell Bi₂WO₆ nanosheets for boosting photocatalytic oxygen evolution, *Appl. Catal. B Environ.* 238 (2018) 119–125.
- [28] X. Zheng, J. Wang, J. Liu, Z. Wang, S. Chen, X. Fu, Photocatalytic degradation of benzene over different morphology BiPO₄: revealing the significant contribution of high-energy facets and oxygen vacancies, *Appl. Catal. B Environ.* 243 (2019) 780–789.
- [29] J. Wang, W. Jiang, D. Liu, Z. Wei, Y. Zhu, Photocatalytic performance enhanced via surface bismuth vacancy of Bi₆S₂O₁₅ core/shell nanowires, *Appl. Catal. B Environ.* 176–177 (2015) 306–314.
- [30] Y. Lu, Y. Yang, X. Fan, Y. Li, D. Zhou, B. Cai, L. Wang, K. Fan, K. Zhang, Boosting charge transport in BiVO₄ photoanode for solar water oxidation, *Adv. Mater.* 34 (2022) 2108178.
- [31] L. Liu, S. Du, X. Guo, Y. Xiao, Z. Yin, N. Yang, Y. Bao, X. Zhu, S. Jin, Z. Feng, F. Zhang, Water-stable nickel metal–organic framework nanobelts for cocatalyst-free photocatalytic water splitting to produce hydrogen, *J. Am. Chem. Soc.* 144 (2022) 2747–2754.
- [32] J.M. Lee, J.H. Baek, T.M. Gill, X. Shi, S. Lee, I.S. Cho, H.S. Jung, X. Zheng, A Zn:BiVO₄/Mo:BiVO₄ homojunction as an efficient photoanode for photoelectrochemical water splitting, *J. Mater. Chem. A* 7 (2019) 9019–9024.
- [33] A. Rubio-Clemente in *Physico-Chemical Wastewater Treatment and Resource Recovery* (Eds.: E. Chica, G. A. Peña, 2017, Chapter 2.
- [34] H. Hirakawa, S. Shiota, Y. Shiraishi, H. Sakamoto, S. Ichikawa, T. Hirai, Au nanoparticles supported on BiVO₄: effective inorganic photocatalysts for H₂O₂ production from water and O₂ under visible light, *ACS Catal.* 6 (2016) 4976–4982.
- [35] W.C. Hou, Y.S. Wang, Photocatalytic generation of H₂O₂ by graphene oxide in organic electron donor-free condition under sunlight, *ACS Sustain. Chem. Eng.* 5 (2017) 2994–3001.
- [36] Z. Wei, M. Liu, Z. Zhang, W. Yao, H. Tan, Y. Zhu, Efficient visible-light-driven selective oxygen reduction to hydrogen peroxide by oxygen-enriched graphitic carbon nitride polymers, *Energy Environ. Sci.* 11 (2018) 2581–2589.
- [37] L. Wang, S. Cao, K. Guo, Z. Wu, Z. Ma, L. Piao, Simultaneous hydrogen and peroxide production by photocatalytic water splitting, *Chin. J. Catal.* 40 (2019) 470–475.
- [38] C. Feng, L. Tang, Y. Deng, J. Wang, J. Luo, Y. Liu, X. Ouyang, H. Yang, J. Yu, J. Wang, Synthesis of leaf-vein-like g-C₃N₄ with tunable band structures and charge transfer properties for selective photocatalytic H₂O₂ evolution, *Adv. Funct. Mater.* 30 (2020) 2001922.
- [39] Z. Teng, Q. Zhang, H. Yang, K. Kato, W. Yang, Y.-R. Lu, S. Liu, C. Wang, A. Yamakata, C. Su, B. Liu, T. Ohno, Atomically dispersed antimony on carbon nitride for the artificial photosynthesis of hydrogen peroxide, *Nat. Catal.* 4 (2021) 374–384.
- [40] Y. Zhao, P. Zhang, Z. Yang, L. Li, J. Gao, S. Chen, T. Xie, C. Diao, S. Xi, B. Xiao, C. Hu, W. Choi, Mechanistic analysis of multiple processes controlling solar-driven H₂O₂ synthesis using engineered polymeric carbon nitride, *Nat. Commun.* 12 (2021) 3701.
- [41] X. Zhang, P. Ma, C. Wang, L. Gan, X. Chen, P. Zhang, Y. Wang, H. Li, L. Wang, X. Zhou, K. Zheng, Unraveling the dual defect sites in graphite carbon nitride for ultra-high photocatalytic H₂O₂ evolution, *Energy Environ. Sci.* 15 (2022) 830–842.
- [42] M. Li, Q. Zheng, D.P. Durkin, H. Chen, D. Shuai, Environmental application of chlorine-doped graphitic carbon nitride: continuous solar-driven photocatalytic production of hydrogen peroxide, *J. Hazard. Mater.* 436 (2022) 129251.
- [43] Z. Li, Y. Zhou, Y. Zhou, K. Wang, Y. Yun, S. Chen, W. Jiao, L. Chen, B. Zou, M. Zhu, Dipole field in nitrogen-enriched carbon nitride with external forces to boost the artificial photosynthesis of hydrogen peroxide, *Nat. Commun.* 14 (2023) 5742.
- [44] Y. Zhang, C. Pan, G. Bian, J. Xu, Y. Dong, Y. Zhang, Y. Lou, W. Liu, Y. Zhu, H₂O₂ generation from O₂ and H₂O on a near-infrared absorbing porphyrin supramolecular photocatalyst, *Nat. Energy* 8 (2023) 361–371.
- [45] T. Liu, Z. Pan, K. Kato, J.J.M. Vequizo, R. Yanagi, X. Zheng, W. Yu, A. Yamakata, B. Chen, S. Hu, K. Katayama, C. Chu, A general interfacial-energetics-tuning strategy for enhanced artificial photosynthesis, *Nat. Commun.* 13 (2022) 7783.
- [46] R. Du, K. Xiao, B. Li, X. Han, C. Zhang, X. Wang, Y. Zuo, P. Guardia, J. Li, J. Chen, J. Arbiol, A. Cabot, Controlled oxygen doping in highly dispersed Ni-loaded g-C₃N₄ nanotubes for efficient photocatalytic H₂O₂ production, *Chem. Eng. J.* 441 (2022) 135999.

- [47] S. Li, G. Dong, R. Hailili, L. Yang, Y. Li, F. Wang, Y. Zeng, C. Wang, Effective photocatalytic H_2O_2 production under visible light irradiation at g- C_3N_4 modulated by carbon vacancies, *Appl. Catal. B Environ.* 190 (2016) 26–35.
- [48] H. Voraberger, V. Ribitsch, M. Janotta, B. Mizaikoff, Application of mid-infrared spectroscopy: measuring hydrogen peroxide concentrations in bleaching baths, *Appl. Spectrosc.* 57 (2003) 574–579.
- [49] F. Dai, Q. Zhuang, G. Huang, H. Deng, X. Zhang, Infrared spectrum characteristics and quantification of OH groups in coal, *ACS Omega* 8 (2023) 17064–17076.
- [50] R.L. Frost, J. Čejka, J. Sejkora, J. Plášil, B.J. Reddy, E.C. Keeffe, Raman spectroscopic study of a hydroxy-arsenate mineral containing bismuth–atelestite $\text{Bi}_2\text{O}(\text{OH})(\text{AsO}_4)$, *Spectrochim. Acta A Mol. Biomol. Spectrosc.* 78 (2011) 494–496.
- [51] R.L. Frost, R. Scholz, F.M. Belotti, A. López, F.L. Theiss, A vibrational spectroscopic study of the phosphate mineral vantasselite $\text{Al}_4(\text{PO}_4)_3(\text{OH})_3 \cdot 9\text{H}_2\text{O}$, *Spectrochim. Acta A Mol. Biomol. Spectrosc.* 147 (2015) 185–192.
- [52] A. Watenphul, C. Schmidt, Calibration of berlinite (AlPO_4) as Raman spectroscopic pressure sensor for diamond-anvil cell experiments at elevated temperatures, *J. Raman Spectrosc.* 43 (2012) 564–570.
- [53] P.A. Giguère, H. Chen, Hydrogen bonding in hydrogen peroxide and water. A Raman study of the liquid state, *J. Raman Spectrosc.* 15 (1984) 199–204.
- [54] K.S. Exner, On the Lattice Oxygen Evolution Mechanism: Avoiding Pitfalls, *ChemCatChem* 13 (2021) 4066–4074.
- [55] W. Li, S. Li, Y. Tang, X. Yang, W. Zhang, X. Zhang, H. Chai, Y. Huang, Highly efficient activation of peroxymonosulfate by cobalt sulfide hollow nanospheres for fast ciprofloxacin degradation, *J. Hazard. Mater.* 389 (2020) 121856.
- [56] D. Awfa, M. Ateia, M. Fujii, C. Yoshimura, Photocatalytic degradation of organic micropollutants: Inhibition mechanisms by different fractions of natural organic matter, *Water Res.* 174 (2020) 115643.
- [57] G.A. Truesdale, A.L. Downing, G.F. Lowden, The solubility of oxygen in pure water and sea-water, *J. Appl. Chem.* 5 (2007) 53–62.
- [58] S.K. Loeb, P.J.J. Alvarez, J.A. Brame, E.L. Cates, W. Choi, J. Crittenden, D. D. Dionysiou, Q. Li, G. Li-Puma, X. Quan, D.L. Sedlak, T. David Waite, P. Westerhoff, J.-H. Kim, The technology horizon for photocatalytic water treatment: sunrise or sunset? *Environ. Sci. Technol.* 53 (2018) 2937–2947.
- [59] J.R. Bolton, K.G. Bircher, W. Tumas, C.A. Tolman, Figures-of-merit for the technical development and application of advanced oxidation technologies for both electric- and solar-driven systems (IUPAC Technical Report), *Pure Appl. Chem.* 73 (2001) 627–637.